

# Further study of $D_s^+$ decays into $\pi^-\pi^+\pi^+$

E. Klempt<sup>1,a</sup>, M. Matveev<sup>1,2</sup>, A.V. Sarantsev<sup>1,2</sup>

<sup>1</sup> Helmholtz-Institut für Strahlen- und Kernphysik, Universität Bonn, Nußallee 14–16, 53115 Bonn, Germany

<sup>2</sup> Petersburg Nuclear Physics Institute, Gatchina, Leningrad district 188300, Russia

Received: 23 July 2007 / Revised version: 29 February 2008 /

Published online: 10 April 2008 – © Springer-Verlag / Società Italiana di Fisica 2008

**Abstract.** A Dalitz plot analysis of the OZI rule violating decay  $D_s^+$  into  $\pi^-\pi^+\pi^+$  is presented using different partial wave approaches. Scalar and vector waves are described by  $K$ -matrices; their production is parameterized in a  $P$ -vector approach. Alternatively, Breit–Wigner amplitudes and Flatté parametrization are used. Special emphasis is devoted to scalar mesons. The  $f_0(980)$  resonance provides the most significant contribution. Adding  $f_0(1500)$  to the scalar wave leads to an acceptable fit while introduction of  $f_0(1370)$  and/or  $f_0(1710)$  does not lead to significant improvements. A scan of the scalar wave optimizes for  $M = 1452 \pm 22 \text{ MeV}/c^2$ . When  $f_0(1710)$  is added, the mass uncertainty increases, and the fit yields  $M = 1470 \pm 60 \text{ MeV}/c^2$  which is fully compatible with the nominal  $f_0(1500)$  mass. The scalar wave seems to exhibit a phase motion of  $270^\circ$  units in the mass range from 1200 to 1650  $\text{MeV}/c^2$ .

**PACS.** 11.80.Et; 13.20.Fc; 14.40.Cs

## 1 Introduction

Decays of charmed mesons provide an efficient tool to study meson-meson interactions at low energies. Outstanding examples are the analyses of the  $D^+ \rightarrow \pi^-\pi^+\pi^+$  Dalitz plot which helped to establish the  $\sigma(500)$  [1], and the two reactions  $D^0 \rightarrow K_S^0\pi^+\pi^-$  [2, 3] and  $D^+ \rightarrow K^-\pi^+\pi^+$  [4–6] which revealed the existence of the  $\kappa(700)$  meson. The reaction  $D_s^+ \rightarrow \pi^-\pi^+\pi^+$  was proven to provide access to mesons in which the primarily formed  $s\bar{s}$  state converts into a  $\pi^-\pi^+$  pair [7–10] in a OZI rule violating transition. In  $D$  and  $D_s$  decays into three pseudoscalar mesons, a large fraction of the cross section is assigned to a pseudoscalar meson recoiling against a scalar meson; this fact makes  $D$  and  $D_s$  decays very well suited for investigations of the spectrum of scalar mesons and their flavor wave function. A survey of data sets and of Dalitz plot analyses of  $D$  and  $D_s$  decays [11] can be found in the Review of Particle Properties [12].

In spite of the large potential for illuminating contributions to our understanding of scalar mesons up to a mass of  $\sim 1700 \text{ MeV}/c^2$ , the situation concerning the states  $f_0(1370)$  and  $f_0(1500)$  and their contributions to the reaction  $D_s^+ \rightarrow \pi^-\pi^+\pi^+$  is still controversial. The evidence for the existence of  $f_0(1370)$  has often been questioned [13–16]; if it exists, the flavor decomposition of the scalar states remains unclear as evidenced by the numerous mixing schemes in which a scalar glueball is supposed to intrude into the spectrum of scalar  $q\bar{q}$  meson, to mix

with them thus creating the observed pattern of scalar resonances. Instead of a ‘narrow’  $f_0(1370)$ , a wide scalar background has been proposed which was called  $f_0(1000)$  by Au, Morgan and Pennington [14], and ‘red dragon’ by Minkowski and Ochs [15]. A survey of different mixing schemes and a critical discussion of their foundations are reported in a recent review [16].

All analyses of  $D_s^+$  decays into  $\pi^-\pi^+\pi^+$  agree on basic features of the data even though different partial wave analysis techniques were applied which led – in important details – to rather different conclusions [7–10]. In all analyses the Dalitz plot is shown to be dominated by  $f_0(980)$ . There is possibly a small contribution from  $\pi^+\rho^0$ ; significant contributions stem from  $\pi^+\rho(1450)$  and  $\pi^+f_2(1270)$ . In the scalar isoscalar partial wave, there is a sizable contribution which leads to a peak at a mass of about  $1450 \text{ MeV}/c^2$ . The origin of this enhancement is however controversial. E791 fitted the  $D_s^+ \rightarrow \pi^+\pi^+\pi^-$  data with a scalar resonance for which  $m_0 = 1434 \pm 18 \pm 9 \text{ MeV}/c^2$  and  $\Gamma_0 = 173 \pm 32 \pm 6 \text{ MeV}/c^2$  were found. They had observed  $f_0(1370)$  production in an analysis of the  $D \rightarrow 3\pi$  Dalitz plot and identified the scalar intensity with  $f_0(1370)$ . The  $f_0(1370)$  is not supposed to have a large  $s\bar{s}$  component, but its production could be assigned to the annihilation diagram (see Fig. 1c). The Focus collaboration reported  $m_0 = 1475 \pm 10 \text{ MeV}/c^2$  and  $\Gamma_0 = 112 \pm 24 \text{ MeV}/c^2$ . These parameters are nearly compatible with  $f_0(1500)$ . Thus, the important issue to which extend the two states  $f_0(1370)$  and  $f_0(1500)$  contribute remained unsettled.

In this paper we report on a further study of the  $D_s^+ \rightarrow \pi^-\pi^+\pi^+$  Dalitz plot. The main point of the analysis is an

<sup>a</sup> e-mail: klempt@hiskp.uni-bonn.de

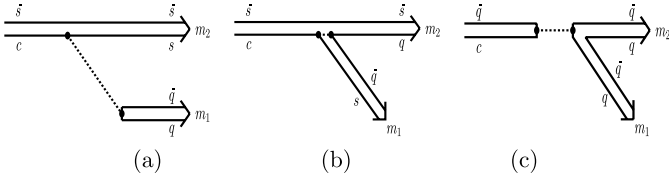


**Fig. 1.** Decays of charmed meson: **a** Leading mechanism. The  $q\bar{q}$  pair can be  $u\bar{d}$  or  $u\bar{s}$ . **b** Color suppressed diagram. The  $q\bar{q}$  pair is likely  $u\bar{d}$ . **c** Annihilation diagram. Here,  $q$  can be  $u, d$  or  $s$  quarks

exploration of different methods and of the impact the analysis technique has on the final result.

The paper is organized as follows. In Sect. 2 we remind the reader of some basic features of weak decays of charmed strange mesons. Subsequently, a short survey is given of the apparatus (Sect. 3), of the data and of data selection. Section 4 contains a description of the amplitudes used to fit the data, and the fit results. The paper ends with a discussion of the results and a short summary.

## 2 Decays of charmed mesons

Before starting a partial wave analysis of  $D_s^+ \rightarrow \pi^-\pi^+\pi^+$  decays (inclusion of the charge conjugate reaction is understood), it may be useful to remind of some properties of weak decays of charmed mesons relevant to light-quark spectroscopy.

Figure 1 depicts Feynman diagrams for the decay of charmed mesons. In Cabibbo favored decays of  $D_s^+$  mesons (Fig. 1a) the primary  $c$  quark converts into an  $s$  quark under emission of a  $W^+$  while the  $\bar{s}$  quark acts as a spectator particle. The most likely decay of the  $W^+$  produces  $\pi^+$ . Conversion of a  $c$  quark into a  $d$  quark or  $W^+$  decay into  $K^+$  are Cabibbo suppressed. Hence most likely, a meson with hidden strangeness emerges, recoiling against a  $\pi^+$ . Evidence for this diagram can be found in a comparison of  $D_s^+ \rightarrow \pi^+\phi$  and  $D_s^+ \rightarrow \pi^+\omega$ . The former reaction occurs with  $(4.4 \pm 0.6) \times 10^{-2}$  frequency, the latter reaction with  $(3.4 \pm 1.2) \times 10^{-3}$ : the reaction  $D_s^+ \rightarrow \pi^+\omega$  is suppressed. The suppression is not as large as expected from  $\phi$ - $\omega$  mixing (for a deviation  $\delta_V \sim 3.5^\circ$  from the ideal mixing angle, a suppression by  $\arctg^{-2}\delta_V \sim 1/250$ ), suggesting other mechanisms to contribute to  $D_s^+ \rightarrow \pi^+\omega$ . These branching fractions and a few further ones are collected in Table 1.

Figure 1b shows a Cabibbo allowed but color suppressed diagram. The two quarks of the  $u\bar{d}$  pair need to

match in color with the  $s$  and the  $\bar{s}$  quark, leading to an expected  $1/N_c$  reduction of the probability. However,  $D_s^+$  mesons are observed to decay into  $K^+\bar{K}^{*0}$  and  $K^{*+}\bar{K}^0$  with a mean rate of  $(7.9 \pm 1.4)\%$ , to be compared with the  $(4.4 \pm 0.6) \times 10^{-2}$  frequency with which  $D_s^+ \rightarrow \pi^+\phi$  is produced. Thus additional processes contributing to production of open strangeness are required.

The annihilation diagram of Fig. 1c contributes to  $D_s^+$  decays with an a priori unknown fraction. The intermediate  $W^+$  may convert into the  $3\pi$  final state via  $\rho\pi^+$  or  $f_2(1270)\pi^+$  but also into a scalar and a pseudoscalar meson.

Evidence for annihilation can be deduced from leptonic decays modes [12].  $D_s^+$  mesons have a large probability to decay into  $\tau^+\nu_\tau$ ; decays into  $\mu^+\nu_\mu$  or  $e^+\nu_e$  are suppressed due to helicity conservation. The  $u, d$  (constituent) quark masses suggest hadronic branching ratios to contribute several % when the number of colors is included.  $D_s^+ \rightarrow \pi^+\omega$  production is thus likely due to the annihilation diagram. The strange mass is of course larger; annihilation could be the reason for the unexpectedly high  $K^+\bar{K}^{*0}$  and  $K^{*+}\bar{K}^0$  yields. Cabibbo and color suppressed decays could also contribute to  $\pi^+\omega$  production by rescattering processes in the final state; these processes are however expected to make at most small contributions.

Large fractional yields in purely pionic final states are observed via production of  $\eta$  and  $\eta'$  in the intermediate state. It is clear why these yields are comparatively large: due to their  $s\bar{s}$  components,  $\eta$  and  $\eta'$  couple strongly to the initial  $s\bar{s}$  system. Their  $n\bar{n}$  component leads to pionic final states. The large yields of scalar mesons in  $D_s^+$  decays points to the presence of both,  $n\bar{n}$  and  $s\bar{s}$  components in the wave functions of scalar mesons.

## 3 Detector and data analysis

### 3.1 The E791 experiment

The data analyzed here have been collected at Fermilab in a 500 GeV/c  $\pi^-$  beam impinging on platinum and carbon targets. The pion beam was tracked in proportional wire chambers (PWC's) and silicon microstrip detectors (SMD's) in front of the targets; particles emerging from a hadronic reaction were detected in a spectrometer which consisted of further PWC's and SMD's, two magnets, 35 drift chamber (DC) planes, two gas Čerenkov counters, an electromagnetic calorimeter, a hadronic calorimeter and a muon detector composed of an iron shield and two planes of scintillation counters. A full description of the detector, of data reconstruction and of data analysis can be found in [8, 17].

In a first analysis stage, events were required to have a reconstructed primary production vertex whose location coincided with one of the target foils. Furthermore, events had to have a well separated secondary decay vertex (more than  $4\sigma_{\text{vertex recon error}}$  in the longitudinal

**Table 1.** Selected  $D_s^+$  decay modes [12]

$D_s^+ \rightarrow \mu^+\nu_\mu$	$(6.1 \pm 1.9) \times 10^{-3}$	$D_s^+ \rightarrow \tau^+\nu_\tau$	$(6.4 \pm 1.5) \times 10^{-2}$
$D_s^+ \rightarrow \pi^+\phi$	$(4.4 \pm 0.6) \times 10^{-2}$	$D_s^+ \rightarrow \pi^+\omega$	$(3.4 \pm 1.2) \times 10^{-3}$
$D_s^+ \rightarrow \pi^+\eta$	$(2.11 \pm 0.35) \times 10^{-2}$	$D_s^+ \rightarrow \pi^+\eta'$	$(4.7 \pm 0.7) \times 10^{-2}$
$D_s^+ \rightarrow \rho^+\eta$	$(13.1 \pm 2.6) \times 10^{-2}$	$D_s^+ \rightarrow \rho^+\eta'$	$(12.2 \pm 2.4) \times 10^{-2}$

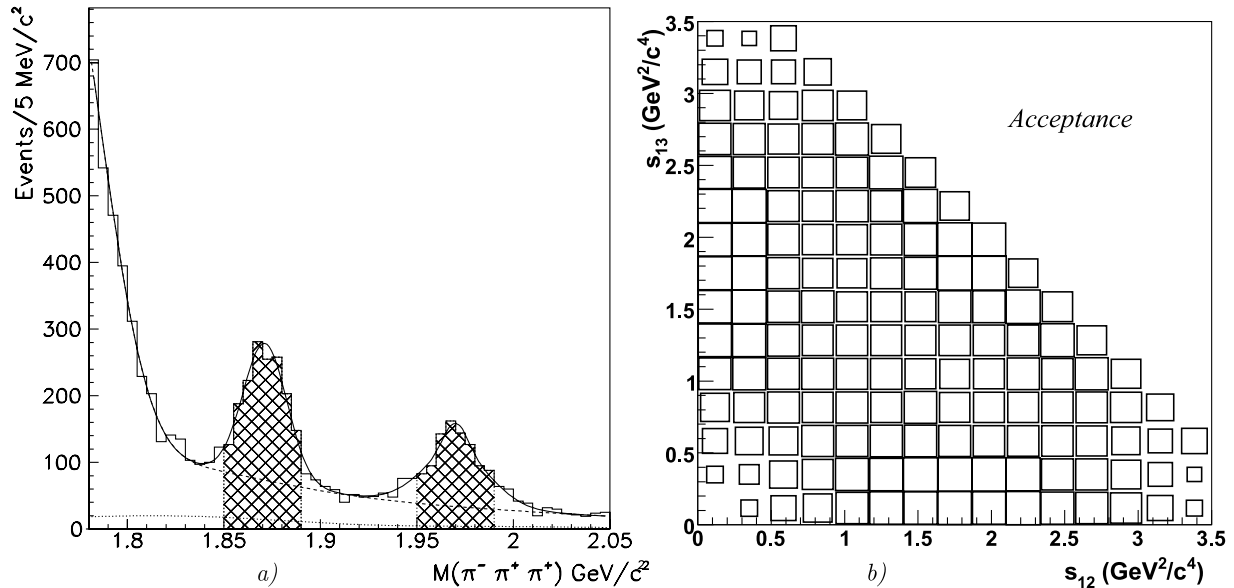


**Fig. 2.** **a** The  $\pi^-\pi^+\pi^+$  invariant mass spectrum. The *dotted line* represents the sum of the expected contributions from  $D^0 \rightarrow K^-\pi^+$  and  $D_s^+ \rightarrow \eta'\pi^+$  decays; the *dashed line* is the total background. Events in the *hatched areas* at the  $D_s$  mass are used in this analysis. The *hatched area* at the  $D^+$  mass was used to establish the  $\sigma(500)$  and its properties. **b** Detector acceptance in the mass range from 1.97 to 1.99  $\text{GeV}/c^2$

separation), and 3 reconstructed tracks with a total charge +1. Particle identification was not required, tracks were assumed to originate from charged pions. The mass distribution of events due to three-pion systems surviving these cuts is shown in Fig. 2 for  $\pi^-\pi^+\pi^+$  invariant masses falling into the 1.7 to 2.1  $\text{GeV}/c^2$  mass bin. The data can be described by two Gaussians at 1.87 and 1.97  $\text{GeV}/c^2$  with resolution  $\sigma_{1.87} = 11.8$  and  $\sigma_{1.97} = 13.5 \text{ MeV}/c^2$ , respectively. For the background function, an exponential form was chosen. There are  $1172 \pm 61$  events due to  $D \rightarrow \pi^-\pi^+\pi^+$  events and  $848 \pm 44$  events due to  $D_s^+ \rightarrow \pi^-\pi^+\pi^+$ .

After a cut in the  $\pi^-\pi^+\pi^+$  invariant mass between 1.95 and 1.99  $\text{GeV}/c^2$  as indicated in Fig. 2a, 937 events are retained for further analysis. The integrated signal to background ratio was estimated to  $\sim 2$ .

### 3.2 The detector acceptance

The detector covers the full solid angle and, to a good approximation, the acceptance is flat over the Dalitz plot. On the other hand, some of the cuts introduce small biases and the exact shape of the acceptance needs to be known. The acceptance was determined from the reconstruction efficiency of  $D_s$  production and decay and the phase space which is smeared out by the finite detector resolution. The reconstruction efficiency was derived by the E791 collaboration using a full Monte Carlo simulation, from the  $\pi-N$  interaction to the digitalization and selection of the events. The generated events had the nominal  $D_s$  mass, the mass distribution of reconstructed events was compatible with the distribution shown in Fig. 2a. For the analysis presented here, this distribution was divided

into 100 slices; then events were generated, for each slice, simulating  $D_s^+ \rightarrow \pi^-\pi^+\pi^+$  decays uniformly spread over the phase space. The summation of all Dalitz plot multiplied with the reconstruction efficiency gave the acceptance  $\text{Acc}(s_{12}, s_{13})$  as presented in Fig. 2b ( $s_{12} = m_{\pi^-\pi^+}^2$ ,  $s_{13} = m_{\pi^-\pi^+}^2$ ). In this way, edge bins are properly taking into account.

### 3.3 The background

The fit in Fig. 2a assigned 568 events to  $D_s$  decays and 280 events to the background. The latter was studied using Monte Carlo simulations. The most prominent background contributions stem from

1. a general combinatorial background,
2.  $D^+ \rightarrow K^-\pi^+\pi^+$  decays where a  $K^+$  is wrongly interpreted as a  $\pi^+$ ,
3.  $D_s^+ \rightarrow \eta'\pi^+$  decays followed by  $\eta' \rightarrow \rho^0(770)\gamma$ ,  $\rho^0(770) \rightarrow \pi^+\pi^-$  with a missing  $\gamma$ ,
4.  $D^0 \rightarrow K^-\pi^+$  decays with an extra track (mostly from the primary vertex).

Amount and shape of the background is determined using both Monte Carlo simulations and data. The contribution of the  $D_s^+ \rightarrow \eta'\pi^+$  background is negligible. The sum of contributions 1, 2, and 3 above,  $\text{Bg}_1$ , populates uniformly the  $D_s^+ \rightarrow \pi^-\pi^+\pi^+$  Dalitz plot region. In the observed Dalitz plot, its distribution is proportional to the acceptance. This latter background represents  $88 \pm 2\%$  of the total background contribution to the Dalitz plot. The shape of the background from  $D^0 \rightarrow K^-\pi^+$  decays,  $\text{Bg}_2$  representing  $12 \pm 2\%$  of the

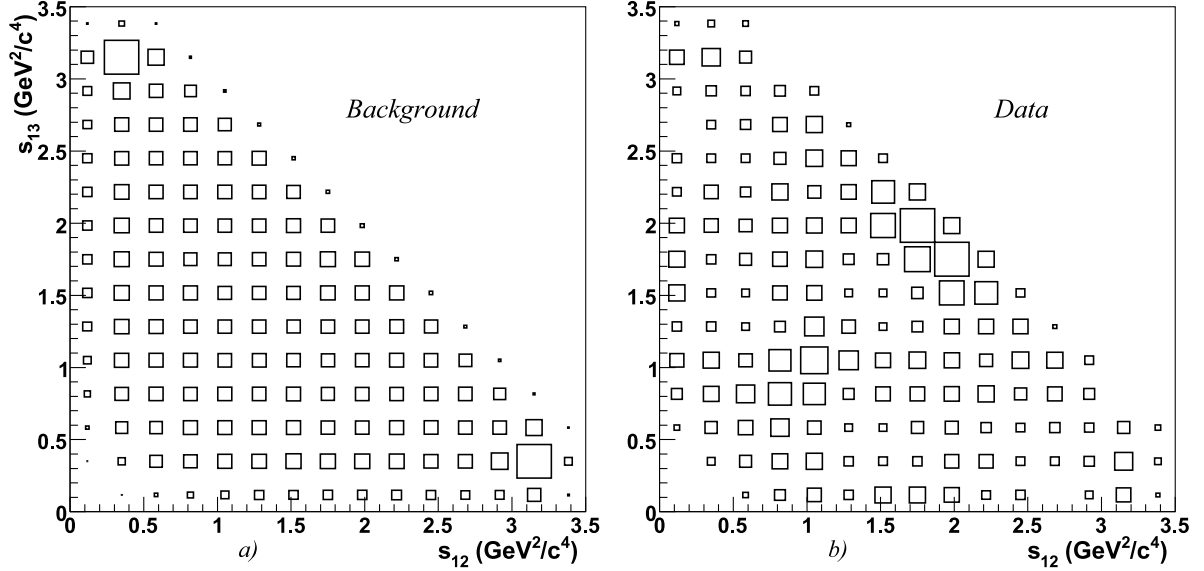


**Fig. 3.** **a** The background Dalitz plot. **b** The  $D_s^+ \rightarrow \pi^-\pi^+\pi^+$  Dalitz plot. Since there are two identical particles, the plot is symmetrized

total background, is taken from simulations. It can be described analytically, the function is reproduced in the second part of the r.h.s. of (1). The total background,  $Bg = Bg_1 + Bg_2$ , is a function of the (symmetrized) Dalitz plot variables:

$$Bg(s_{12}, s_{13}) = 1.103 \text{Acc}(s_{12}, s_{13}) + 0.0065 \times (g_{D_0}(s_{12}, s_{13}) + g_{D_0}(s_{13}, s_{12})) / 2, \quad (1)$$

where

$$g_{D_0}(s_{12}, s_{13}) = 7.2343 e^{-0.5((0.25-s_{12})/0.2)^2 + ((3.15-s_{13})/0.11)^2}.$$

After summation over the Dalitz plot, the background  $Bg_1$  ( $Bg_2$ ) represents 246 (34) events. The Dalitz plot distribution of the total background is shown in Fig. 3a.

### 3.4 The $D_s^+ \rightarrow \pi^-\pi^+\pi^+$ Dalitz plot

The symmetrized Dalitz plot for the  $D_s^+$  candidates shown in Fig. 3b is reproduced from [8]. Since the two  $\pi^+$  are identical, the Dalitz plot is symmetrized. To avoid problems with statistical errors, all entries receive a weight  $\frac{1}{2}$ .

The most striking features of the Dalitz plot are the narrow horizontal and vertical bands just below  $s_{12} \simeq s_{13} \simeq 1 \text{ GeV}^2/c^4$  and a complex structure at  $2 \text{ GeV}^2/c^4$ . The bands correspond to  $f_0(980)\pi_{(1)}^+$  decays, with  $f_0(980) \rightarrow \pi_{(2)}^+\pi^-$ . The two  $\pi^+$  are identical; two interfering amplitudes contribute to the final state. The structure at  $2 \text{ GeV}^2/c^4$  contains contributions from  $f_2(1270)\pi^+$ , from  $\rho^0(1460)\pi^+$ , and from  $\pi^+$  recoiling against scalar intensity. The clarification of this structure is the prime aim of this paper.

## 4 Partial wave analysis

### 4.1 The fit function

The partial wave analysis describes the Dalitz plot of Fig. 3b by a summation over possible reaction mechanisms for  $D_s^+ \rightarrow 2\pi^+\pi^-$  decays plus background contributions. The different reaction mechanisms can interfere, hence they are represented by amplitudes. We consider the following reactions:

1. a  $\pi^+$  recoiling against  $\pi^+\pi^-$  in  $S$ -wave;
2. a  $\pi^+$  recoiling against  $\pi^+\pi^-$  in  $P$ -wave;
3. a  $\pi^+$  recoiling against  $\pi^+\pi^-$  in  $D$ -wave.

The  $D$ -wave is always described by a  $f_2(1270)$  Breit-Wigner amplitude. The  $S$ - and  $P$ -waves are alternatively represented by a sum of two-channel Breit-Wigner amplitudes or by  $K$ -matrices. Isotensor interactions are not included.

Due to Bose symmetry, the amplitudes are symmetrized with respect to the exchange of the two  $\pi^+$  mesons. We use the following notations:  $P = k_1 + k_2 + k_3$  is the momentum of the  $D_s^+$  meson ( $P^2 = s$ );  $k_1$ ,  $k_2$  and  $k_3$  are the pion momenta of the  $\pi^-$  and of the two  $\pi^+$ . Obviously,  $k_1^2 = k_2^2 = k_3^2 = m_\pi^2$  holds. The amplitude depends of two invariant energy variables:

$$s_{12} = (k_1 + k_2)^2 \quad \text{and} \quad s_{13} = (k_1 + k_3)^2. \quad (2)$$

The total amplitude includes contributions of different partial waves ( $S$ -,  $P$ - and  $D$ -waves); it can be written in the form

$$\mathcal{A}_{\text{tot}}(s_{12}, s_{13}) = \sum_{\alpha} [Z(k_1, k_3)\mathcal{A}_{\alpha}(s_{12}) + Z(k_1, k_2)\mathcal{A}_{\alpha}(s_{13})], \quad (3)$$

where  $Z$  is a function referring to the spin–orbital angular momentum structure of the two mesons emerging from the decays of an intermediate state. For scalar, vector and tensor waves, they have the following form ( $i = 2, 3$ ):

$$\begin{aligned} Z_S(k_1, k_i) &= 1, & Z_V(k_1, k_i) &= z_{1i}, \\ Z_T(k_1, k_i) &= \frac{1}{2}(3z_{1i}^2 - 1), & z_{1i} &= \frac{k_{10}k_{30} - (k_1 k_i)}{|\mathbf{k}_1||\mathbf{k}_i|}. \end{aligned} \quad (4)$$

The amplitude contains the summation over the different isobars. Each isobar depends on free fit parameters like masses, widths and coupling constants.

The intensity observed in the Dalitz plot is proportional to the squared reaction amplitude, to the phase space density  $\Phi$  for  $D_s$  decays and the background, and to the detector acceptance  $\text{Acc}$ .

$$N(s_{12}, s_{13}) = |\mathcal{A}_{\text{tot}}(s_{12}, s_{13})|^2 \text{Acc}(s_{12}, s_{13}) \Phi_{D_s} + \alpha(\text{Bg}_1(1 - \beta) + \beta\text{Bg}_2)\Phi_{\text{Bg}}. \quad (5)$$

The two background functions are given in (1). Note that the background definition includes the acceptance.

For the amplitude  $\mathcal{A}_{\text{tot}}(s_{12}, s_{13})$  we use different approaches. The scalar amplitude contains a choice of a series of poles for  $\sigma(500)$ ,  $f_0(980)$ ,  $f_0(1370)$ ,  $f_0(1500)$ , and  $f_0(1710)$ . The vector amplitude comprises up to three poles at 770, 1460 and 1740 MeV/ $c^2$ . The tensor wave is described by a Breit–Wigner amplitude for the  $f_2(1270)$  meson. In most cases, we use fixed masses and widths.

As dynamical function describing meson resonances, we use  $K$ -matrices or relativistic Breit–Wigner amplitudes.

1. In a first approach, we use  $K$ -matrices to describe scalar resonances. For vector mesons, either a  $K$ -matrix or Breit–Wigner functions are introduced.
2. In the second method, the  $f_0(980)$  is represented by the Flatté formula. The total amplitude is formed as a sum of Flatté and Breit–Wigner amplitudes.

## 4.2 Breit–Wigner formalism

### 4.2.1 Breit–Wigner amplitudes

The use of Breit–Wigner amplitudes offers large flexibility and good control of the fit ingredients. The price is the violation of unitarity when two Breit–Wigner amplitudes overlap.

In the Breit–Wigner approach, the dynamical amplitude  $\mathcal{A}_{\text{tot}}(s_{12}, s_{13})$  is given by a sum of relativistic Breit–Wigner amplitudes which can be written in the form

$$\begin{aligned} \mathcal{A}_R &= \text{BW}_R(s) = \frac{\lambda_R^{\pi\pi}}{M_R^2 - s - i\Gamma M_R} \\ \Gamma &= \Gamma_R \left( \frac{p}{p_R} \right)^{2L} \left( \frac{\rho}{\rho_R} \right) B'_L(p, p_R), \end{aligned} \quad (6)$$

where  $M_R$  is the mass and  $\Gamma_R$  the partial width of the resonance  $R$ . The complex number  $\lambda_R^{\pi\pi} = A_{D_s^+\pi} g_{\pi\pi}$  is

given by the product of the production amplitude  $A_{D_s^+\pi}$  of the resonance  $R$  in  $D_s$  decays, and the coupling constant  $g_{\pi\pi}$  for its decay into  $\pi\pi$ . The (running) decay momentum is  $p = \frac{1}{2}\sqrt{(s - 4m_\pi^2)}$  while the decay momentum at the nominal mass of the resonance is given by  $p_R = \frac{1}{2}\sqrt{(M_R^2 - 4m_\pi^2)}$ . The phase space is written as  $\rho(s) = \sqrt{(s - 4m_\pi^2)}/s$  and  $\rho_R(M_R^2) = \sqrt{(M_R^2 - 4m_\pi^2)}/M_R^2$ , respectively.

For the three lowest orbital angular momenta, the Blatt–Weisskopf factors  $B'_L$  have the form

$$\begin{aligned} B'_0(p, p_R) &= 1 & B'_1(p, p_R) &= \sqrt{\frac{1 + z_R}{1 + z}} \\ B'_2(p, p_R) &= \sqrt{\frac{(z_R - 3)^2 + 9z_R}{(z - 3)^2 + 9z}}, \end{aligned} \quad (7)$$

where  $z = (|p|d)^2$  is the meson radius. In the fits, the scale parameter  $d$  is restricted to  $d \leq 0.8$  fm.

### 4.2.2 The Flatté parametrisation

The  $f_0(980)$  is taken into account using the Flatté parametrisation

$$\text{BW}_{f_0(980)}(s) = \frac{\lambda_{f_0(980)}^{(\pi\pi)} + i\rho_{K\bar{K}}\lambda_{f_0(980)}^{(K\bar{K})}}{M_{f_0(980)}^2 - s - ig_\pi^2\rho_{\pi\pi} - ig_K^2\rho_{K\bar{K}}}, \quad (8)$$

where  $M_{f_0(980)}$  and  $\Gamma_{f_0(980)}$  are the  $f_0(980)$  mass and width,  $\lambda_{f_0(980)}^{(\pi\pi)}$  and  $\lambda_{f_0(980)}^{(K\bar{K})}$  are complex numbers. The first number ( $\lambda^{\pi\pi}$ ) is the same as the one used in the Breit–Wigner parametrization. The second expression ( $\lambda^{K\bar{K}}$ ) refers to non-resonant two-kaon production and rescattering into  $\pi\pi$ . The coupling constants for  $f_0(980)$  decay into  $\pi\pi$  and  $K\bar{K}$  are denoted as  $g_\pi$  and  $g_K$ ; the two-particle phase space is written as  $\rho_{\pi\pi} = \sqrt{(s - 4m_\pi^2)}/s$  and  $\rho_{K\bar{K}} = \sqrt{(s - 4m_K^2)}/s$ .

### 4.2.3 Parameters of resonances

The  $T$ -matrix poles of the most important resonances are listed in Tables 2 and 3. In most of the fits described below, masses, widths and some coupling constants are frozen.

**Table 2.** The  $\rho_0(1450)$  and  $f_2(1270)$  mass and width ( $M + i\frac{\Gamma}{2}$ )

$\rho_0(1450)$	$f_2(1270)$
1460 + i150	1275 + i92.5

**Table 3.** Masses and widths ( $M + i\frac{\Gamma}{2}$  in GeV/ $c^2$ ) of scalar resonances used in fits

$\sigma(500)$	$f_0(1370)$	$f_0(1500)$	$f_0(1710)$
0.55 + i200	1.32 + i155	1.490 + i58.0	1.769 + i170

The  $f_0(980)$  is described by the Flatté formula; the following parameters are used [18]:

$$M_{f_0(980)} = 1.023 \text{ GeV};$$

$$g_\pi^2 = (0.15 - 0.20) \text{ GeV}^2; \quad \frac{g_K^2}{g_\pi^2} = 2.4. \quad (9)$$

In all cases, we keep the names of Particle Data Group even though we assign different masses to the particles.

### 4.3 $K$ -matrix approach

#### 4.3.1 The formalism

As reference fit, we use a  $K$ -matrix in the  $P$ -vector approach of Anisovich and Sarantsev [18], applied to the analysis of  $D$  and  $D_s$  decays in [9]. The  $S$ -wave amplitude has the form:

$$\mathcal{A}_i(s_{12}) = \frac{P_j(s_{12})}{I - i\rho_{ij}K_{ij}(s_{12})}, \quad (10)$$

where

$$P_j(s_{12}) = \sum_\alpha \frac{\Lambda_\alpha g_j^\alpha}{M_\alpha^2 - s_{12}} + d_j$$

$$K_{ij}(s_{12}) = \left\{ \sum_\alpha \frac{g_i^\alpha g_j^\alpha}{M_\alpha^2 - s_{12}} + f_{ij}^{\text{scatt}} \frac{1 \text{ GeV}^2 - s_0^{\text{scatt}}}{s_{12} - s_0^{\text{scatt}}} \right\}$$

$$\times \frac{(s_{12} - s_A m_\pi^2/2)(1 - s_{A0})}{(s_{12} - s_{A0})} + c_{ij}.$$

The production of a two-meson intermediate state  $j$  is enhanced due to formation of resonances. The summation in (10) extends over all considered scalar resonances  $\alpha$  with mass  $M_\alpha$ . The enhancement is proportional to their production strengths  $\Lambda_\alpha$  (for which we use  $S_\alpha$ ,  $V_\alpha$ , and  $T_\alpha$  to denote the strength to produce scalar, vector or tensor resonances), and their couplings  $g_j^\alpha$  to the decay channel  $j$ . The constants  $d_j$  allow for nonresonant production of that channel; however, this flexibility is not exploited in this paper. The rescattering series is summed up in the  $K$ -matrix. Transitions from unobserved channels  $i$  into the observed channel  $j$  by resonant rescattering are included, nonresonant meson-meson scattering processes are taken into account by matrix elements  $c_{ij}$ . The  $\rho_{ij}$  form the phase space matrix elements:

$$\rho_{ij} = \frac{1}{s} \sqrt{(s - (m_i + m_j)^2)(s - (m_i - m_j)^2)}. \quad (11)$$

The rescattering process  $K\bar{K} \rightarrow \pi\pi$  is allowed below the  $K\bar{K}$  threshold; in this kinematical region,  $\rho_{ij}$  becomes imaginary. The parameters  $f_{ij}^{\text{scatt}}$  and  $s_0^{\text{scatt}}$  describe a slowly varying part of the  $K$ -matrix elements. The masses  $M_\alpha$  and the couplings  $g_j^\alpha$ ,  $f_{ij}^{\text{scatt}}$  are process-independent properties; they were determined in [18] from a large number of data sets and enter as fixed parameters into the analysis presented here. The constants  $\Lambda_\alpha$  and  $d_j$

determine the dynamics of a production process; they are free parameters to be determined from the fits.

In a scattering situation, chiral perturbation theory forces the  $\pi\pi$  amplitude to vanish at small energies. This is a kinematical effect which is not enforced in production. The suppression of the  $\pi\pi$  scattering amplitude at small energies is taken into account by the Adler-Weinberg zero,  $(s - s_{A0} m_\pi^2/2)(1 - s_{A0})/(s - s_{A0})$ . We choose  $s_A = 1$ ,  $s_{A0} = -0.15$ .

For higher partial waves, only the resonant terms are required to describe data. The  $K$ -matrix now contains Blatt-Weisskopf barrier factors  $B_L$

$$K_{ij}(s_{12}) = \sum_\alpha \frac{1}{B_{L(ij)}'} \frac{g_i^\alpha g_j^\alpha}{M_\alpha^2 - s_{12}} \frac{1}{B_{L(ij)}'},$$

which depend on the orbital angular momentum  $L$  between the two mesons, the c.m.s. momentum of the two mesons in the initial and final state and one scale parameter. The Blatt-Weisskopf factors are given in (7). The production vector for channel  $P_j$  is multiplied by one Blatt-Weisskopf factor taking into account the angular momentum barrier for channel  $j$ .

In this paper, the  $K$ -matrix from [18] is used for the  $S$ -wave which included five resonances. These five resonances are observed when the  $T$ -matrix poles of the scattering amplitude are inspected. The  $T$  matrix is defined by

$$T = (I - iK\rho)^{-1}K. \quad (12)$$

The  $T$ -matrix poles depend on the  $K$ -matrix masses and the couplings  $g_j^\alpha$  and are thus independent of the production process. The poles were identified with  $f_0(980)$ ,  $f_0(1370)$ ,  $f_0(1500)$ ,  $f_0(1710)$  of the Particle Data Listings [12] plus a broad resonance  $f_0(1470)$  which was interpreted as scalar glueball.

$K$ -matrix masses and coupling constants  $g_j^\alpha$  and  $f_{ij}^{\text{scatt}}$  are taken from [18]; the values are reproduced in Tables 4 and 5 for two cases. In Table 4, a solution is given which includes a pole for  $f_0(1370)$ ; the parameters in Table 5 are optimized for the case where  $f_0(1370)$  is omitted. The  $K$ -matrix parameters reproduce the  $T$ -matrix poles given in Tables 2 and 3.

**Table 4.**  $K$ -matrix parameters for the scalar isoscalar wave using 5  $K$ -matrix poles. Masses and coupling constants are in GeV. Only the  $i = 1$   $f_{ij}^{\text{scatt}}$  terms are listed since they are the only values relevant to the three-pion decay

$m_\alpha$	$g_{\pi\pi}$	$g_{K\bar{K}}$	$g_{4\pi}$	$g_{\eta\eta}$	$g_{\eta\eta'}$
0.65100	0.22889	-0.55377	0.00000	-0.39899	-0.34639
1.20360	0.94128	0.55095	0.00000	0.39065	0.31503
1.55817	0.36856	0.23888	0.55639	0.18340	0.18681
1.21000	0.33650	0.40907	0.85679	0.19906	-0.00984
1.82206	0.18171	-0.17558	-0.79658	-0.00355	0.22358
$s_0^{\text{scatt}}$	$f_{11}^{\text{scatt}}$	$f_{12}^{\text{scatt}}$	$f_{13}^{\text{scatt}}$	$f_{14}^{\text{scatt}}$	$f_{15}^{\text{scatt}}$
-3.92637	0.23399	0.15044	-0.20545	0.32825	0.35412

**Table 5.**  $K$ -matrix parameters for the scalar isoscalar wave using 4  $K$ -matrix poles. The pole representing  $f_0(1370)$  was omitted resulting, in [18], in a increased  $\chi^2$ . Masses and coupling constants are in GeV

$m_\alpha$	$g_{\pi\pi}$	$g_{KK}$	$g_{4\pi}$	$g_{\eta\eta}$	$g_{\eta\eta'}$
0.69566	0.66859	-0.71636	0.00000	-0.10133	-0.17721
1.24458	0.87180	0.59038	0.00000	0.38115	0.39085
1.54280	0.36228	0.24167	0.50442	0.15035	0.45126
1.84274	0.07290	-0.10118	-0.30778	0.03018	-0.17852
$s_0^{\text{scatt}}$	$f_{11}^{\text{scatt}}$	$f_{12}^{\text{scatt}}$	$f_{13}^{\text{scatt}}$	$f_{14}^{\text{scatt}}$	$f_{15}^{\text{scatt}}$
-3.84414	0.54458	-0.10980	-0.55817	0.46870	-0.02877

**Table 6.**  $K$ -matrix parameters for the vector isovector wave. Masses and coupling constants are in GeV,  $d$  is given in fm. Only the  $i = 1$   $c_{ij}$  terms are listed since they are the only values relevant to the three-pion decay

$m_\alpha$	$d$	$g_{\pi\pi}$	$g_{4\pi}$	$g_{\pi\omega}$
0.77873	0.34469	0.69461	-0.50000	0.00000
1.50000	0.80000	-0.20000	0.54000	-0.65181
1.90000	0.80000	0.18042	-0.71729	-0.30664

For the vector mesons, a  $K$ -matrix is used which contains  $\rho(770)$ ,  $\rho(1450)$ , and  $\rho(1770)$ . The  $K$ -matrix masses and coupling constants are reproduced in Table 6.

## 4.4 Fit results

### 4.4.1 Study of vector and tensor contributions

Our fit strategy is as follows: we first describe the  $S$ -wave and  $P$ -waves using the  $K$ -matrices with fixed pole struc-

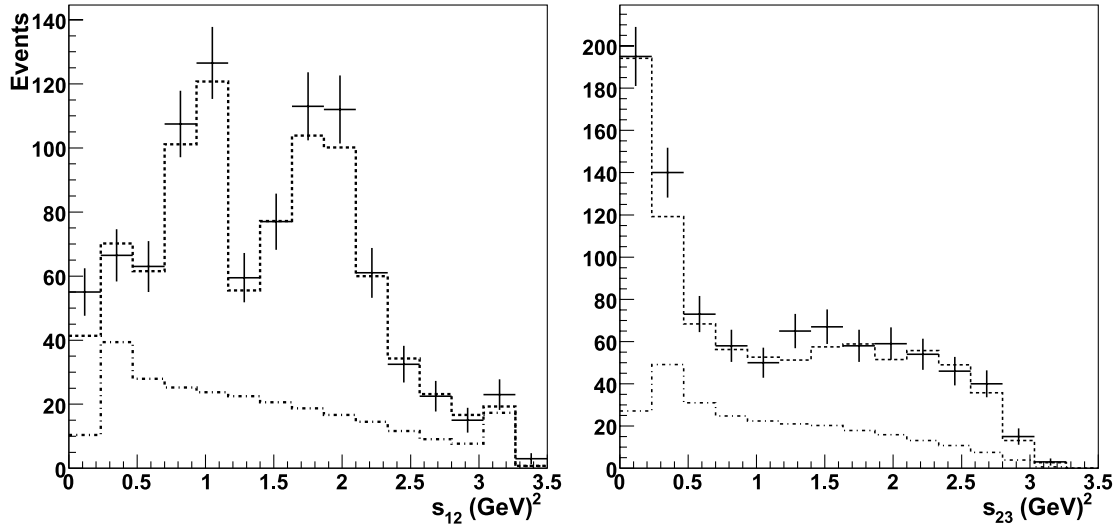


**Fig. 4.** The experimental mass distributions are compared with the Reference fit (solution 1 of Table 7) to  $D_s^+ \rightarrow \pi^+\pi^+\pi^-$  decays

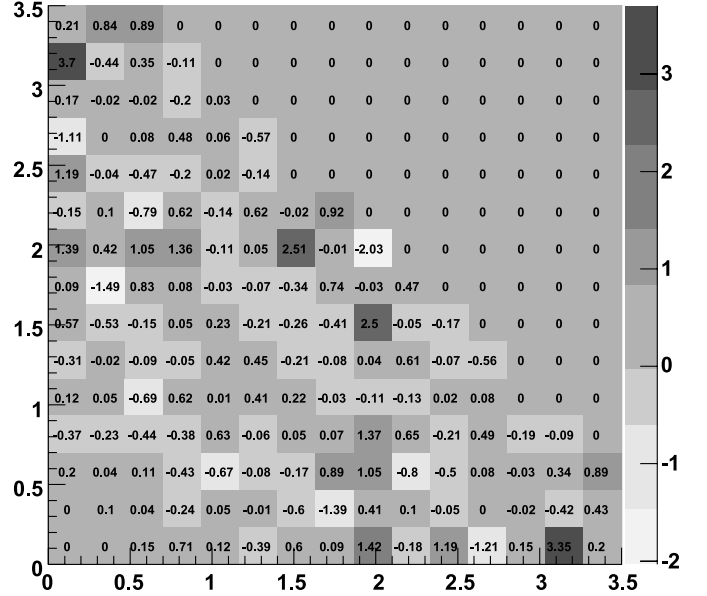


**Fig. 5.** Reference fit (solution 1 of Table 7) to the data  $D_s^+ \rightarrow \pi^+\pi^+\pi^-$ . The  $\chi^2$  contributions of the individual Dalitz plot cells are given in a grey scale and in numbers. For data exceeding the fit, the cells are dark and the  $\chi^2$  is plotted with a positive sign. When the fit exceeds data, the cells are white and  $\chi^2$  is plotted with a negative sign

ture as given in Tables 4 and 6. The  $f_2(1270)$  is included as Breit–Wigner resonance. This fit has 13 parameters to describe the 77 independent cells. Hence there are 64 degrees freedom. The  $\chi^2$  of the fit is 63.49; the fit quality is very satisfactory. Figures 4 and 5 show mass square distributions and, respectively, the  $\chi^2$  per Dalitz plot cell. A negative sign is attached to the  $\chi^2$  whenever the fit result exceeds data.

Results of this fit and the  $\chi^2$  achieved is given in Table 7 as solution 1 (Sol. 1). The (complex) production ampli-

**Table 7.** Fit parameters for five different solutions exploring the role of vector and tensor resonances. The full  $\pi\pi$   $S$ -wave is always included.  $S_1$  and  $S_2$  interfere to make the  $f_0(980)$ ,  $S_3 = f_0(1370)$ ,  $S_4 = f_0(1500)$ ,  $S_5 = f_0(1710)$ . There are up to three vector resonances,  $V_1 = \rho(770)$ ,  $V_2 = \rho(1450)$ , and  $V_3 = \rho(1770)$ , and the tensor  $T_1 = f_2(1270)$ . Given are the complex production strengths  $A_\alpha$  of (10) and the  $\chi^2$  of the fit

	Sol. 1	Sol. 2	Sol. 3	Sol. 4	Sol. 5
$S_1$	8.10 - i5.03	8.61 - i3.80	8.70 - i3.68	6.68 - i6.37	6.78 - i6.31
$S_2$	-7.83 + i2.25	-7.71 + i1.76	-7.73 + i1.64	-7.54 + i3.36	-7.55 + i3.29
$S_3$	-1.81 + i5.46	-2.34 + i6.85	-2.54 + i6.49	-2.01 + i9.66	-1.82 + i9.28
$S_4$	-2.22 + i5.95	-1.78 + i7.53	-2.55 + i6.94	-1.10 + i11.69	-0.75 + i11.21
$S_5$	4.94 - i6.13	6.82 - i7.85	6.91 - i7.10	12.70 - i10.78	11.63 - i10.70
$V_1$	0.10 + i0.14	-0.06 - i0.12	-	0.04 - i0.04	-
$V_2$	3.00 - i15.03	2.86 - i0.23	2.84 - i0.29	2.22 + i0.75	2.15 + i0.85
$V_3$	7.98 - i7.76	-3.08 + i0.61	-2.90 + i0.69	-	-
$T_1$	-5.43 + i0.00	-5.30 + i0.00	-5.31 + i0.00	-5.623 + i0.000	-5.58 + i0.00
$\chi^2$	63.49	62.54	62.75	64.29	64.41

tudes are given without errors; the statistical errors are small in comparison to the spread of results when the fit hypothesis is varied.

In a next step we explore the role of vector and tensor mesons maintaining the full flexibility of the  $S$ -wave description. First, we replace the  $K$ -matrix by three Breit-Wigner amplitudes. A slightly improved  $\chi^2$  is obtained,  $\delta\chi^2 = -0.85$  (Sol. 2). The results do not change significantly when  $\rho(770)$  is removed from the fit. Without  $\rho(770)$ ,  $\chi^2$  increases by 0.21 compared to solution 2, the number of parameters by 2 (Sol. 3). Removing  $\rho(1770)$  changes  $\chi^2$  by 1.75 (Sol. 4), and removing both,  $\rho(770)$  and  $\rho(1770)$ , leads to  $\chi^2 = 64.41$  (Sol. 5), an increase in  $\chi^2$  by about 2 units while four parameters are spared. We conclude that  $\rho(1460)$  is sufficient to describe the contribution of vector mesons to the data. However, if the latter resonance or the  $f_2(1270)$  is taken out of the fit,  $\chi^2$  increases by 20 or more. Both these resonances are required to get a good fit. A further small improvement is achieved when mass and width of the  $\rho$  and  $f_2$  resonances are allowed to vary freely. The resulting values remain compatible with PDG values. Both are included with fixed values for mass and width in all subsequent fits (see Table 2). We note that some fits prefer to split  $\rho(1450)$  into a  $\rho(1250)$  and

a  $\rho(1500)$  even though the statistical evidence for the split  $\rho(1450)$  is weak ( $\delta\chi^2 = 4$  for two more parameters).

#### 4.4.2 Study of the scalar partial wave

Table 8 presents a series of fits in which amplitudes contributing to the  $\pi\pi$   $S$ -wave are explored. For convenience of the reader we reproduce solution 5 of Table 7 as solution 6 in Table 8. We then add a constant  $N_1 = d_{\pi\pi}$  describing direct  $\pi\pi$  production. This gives an improvement of 2.67 in  $\chi^2$  (Sol. 7). Direct production of a  $K\bar{K}$  pair ( $N_2$ ) and subsequent rescattering into  $\pi\pi$  is unimportant:  $\chi^2$  changes by 0.32 units only (Sol. 8).

We now take out  $f_0(1370)$ . This is an alternative solution presented in [18]. In a fit to a large number of reactions, the omission of  $f_0(1370)$  resulted in a worse  $\chi^2$ . The  $K$ -matrix parameters obtained in that fit are listed in Table 5. In the fit to the  $D_s^+ \rightarrow \pi^+\pi^+\pi^-$  data,  $\chi^2$  changes by 6.44 units when solutions 6 (with parameter  $N_1 = 0$ ) is compared to solution 9, and by 4.38 when solution 7 with  $N_1 \neq 0$  is compared to solution 10, see Table 8. Including  $N_2$  in the fit with no  $f_0(1370)$  gives again a marginal improvement.

In a next set of fits, we used the Flatté parametrization to describe the  $f_0(980)$ , and Breit-Wigner amplitudes for

**Table 8.** Study of the scalar wave in the  $K$ -matrix approach. See caption of Table 7

	Sol. 6	Sol. 7	Sol. 8	Sol. 9	Sol. 10
$S_1$	6.78 - i6.31	6.50 - i4.39	6.81 - i4.22	9.05 - i1.07	8.42 - i2.19
$S_2$	-7.55 + i3.23	-7.78 + i2.31	-5.39 - i0.13	-8.73 + i0.53	-9.71 + i0.36
$S_3$	-1.82 + i9.28	0.88 + i4.43	0.45 - i1.418	-1.79 + i1.49	-2.51 - i0.62
$S_4$	-0.75 + i11.21	2.68 + i4.32	-1.18 - i2.64	-	-
$S_5$	11.63 - i10.70	2.68 - i11.03	-0.02 - i3.52	10.97 - i3.34	4.73 - i7.80
$N_1$	-	-1.71 + i4.12	-2.41 + i6.10	-	0.05 + i4.69
$N_2$	-	-	-1.30 + i12.76	-	-
$V_2$	2.15 + i0.85	2.86 + i0.29	2.80 + i0.37	1.70 + i0.20	2.58 - i0.25
$T_1$	-5.58 + i0.00	-5.07 + i0.00	-4.92 + i0.00	-5.39 + i0.00	-5.05 + i0.00
$\chi^2$	64.41	61.74	61.42	70.85	66.12

**Table 9.** Fits using Breit–Wigner amplitudes and Flatté parametrization for  $f_0(980)$ .  $S_1 = \sigma(500)$ ; the two lines for  $f_0(980)$ ,  $S_2$  and  $S_2'$ , give the couplings  $\lambda^{\pi\pi}$  and  $\lambda^{K\bar{K}}$ .  $S_3 = f_0(1370)$ ,  $S_4 = f_0(1500)$ ,  $S_5 = f_0(1710)$ ,  $V_2 = \rho(1450)$ ,  $T_1 = f_2(1270)$

	Sol. 11	Sol. 12	Sol. 13	Sol. 14	Sol. 15
$S_1$	0.73 – i0.14	–	–	–	–
$S_2$	3.57 + i5.18	0.09 + i5.35	1.99 + i3.03	1.66 + i4.48	1.45 + i5.79
$S_2'$	2.53 + i4.94	–4.62 + i3.27	–3.59 + i0.45	–2.78 + i3.10	–1.73 + i5.93
$S_3$	0.96 – i0.58	–	–2.13 – i1.57	–	–
$S_4$	0.71 – i0.71	–	–	0.38 – i0.98	–
$S_5$	4.31 – i1.36	–	–	–	3.76 + i2.09
$V_2$	2.79 + i1.89	0.11 + i3.02	1.28 + i1.96	1.07 + i2.46	1.38 + i2.94
$T_1$	–5.39 + i0.00	–5.77 + i0.00	–5.89 + i0.00	–5.45 + i0.00	–5.40 + i0.00
$\chi^2$	62.47	110.18	78.48	70.56	81.40

**Table 10.** Fits using Breit–Wigner amplitudes and Flatté parametrization for  $f_0(980)$ . See caption of Table 9

	Sol. 16	Sol. 17	Sol. 18	Sol. 19	Sol. 20
$S_1$	0.73 – i0.14	–	–	–	–
$S_2$	3.57 + i5.18	1.39 + i4.12	1.76 + i4.10	1.77 + i3.27	1.78 + i3.76
$S_2'$	2.53 + i4.94	–1.33 + i2.50	–1.17 + i1.87	–2.60 + i2.26	–2.97 + i2.00
$S_3$	0.96 – i0.58	–0.15 + i0.67	–	–2.03 – i0.38	–0.81 – i0.40
$S_4$	0.71 – i0.71	0.66 – i0.61	0.56 – i0.70	–	0.29 – i0.75
$S_5$	4.31 – i1.36	2.72 – i0.92	2.15 – i1.35	2.34 + i1.82	–
$V_2$	2.79 + i1.89	1.82 + i1.83	1.85 + i1.82	1.97 + i1.89	1.27 + i2.15
$T_1$	–5.39 + i0.00	–5.55 + i0.00	–5.55 + i0.00	–5.80 + i0.00	–5.61 + i0.00
$\chi^2$	62.47	65.53	65.97	73.20	69.30

all other resonances. The three states  $f_0(980)$ ,  $\rho(1450)$ , and  $f_2(1270)$  are always included. For the  $S$ -wave, the maximal set of resonances includes, apart from  $f_0(980)$ , the  $\sigma(500)$ ,  $f_0(1370)$ ,  $f_0(1500)$ , and  $f_0(1710)$ . All masses and widths are fixed to the  $T$ -matrix pole positions obtained in [18]. Fit results are collected in Tables 9 and 10.

A fit which includes all resonances (Sol. 11) yields the best  $\chi^2$ , 62.47 for 16 parameters. The  $f_0(980)$  is not sufficient to describe the scalar intensity: when  $\sigma(500)$ ,  $f_0(1370)$ ,  $f_0(1500)$ , and  $f_0(1710)$  are removed,  $\chi^2$  increases dramatically to 110.18 (Sol. 12). The fit is unacceptable. We now test the  $\chi^2$  changes when only one of the three high-mass resonances is included in the fit. Inclusion of  $f_0(1500)$  gives the smallest yield and the largest  $\chi^2$  gain (Sol. 14). The other two resonances (Sol. 13 and 15) need a large yield (to describe intensity at the wrong mass) and bring a smaller gain in  $\chi^2$ . We conclude that  $f_0(1500)$  helps best to describe the data efficiently.

Fit 16 reproduces the results of solution 11. Removing  $S_1 = \sigma(500)$  changes  $\chi^2$  by 3.06 units, and saves two parameters (Sol. 17). The  $\chi^2$  change is certainly not sufficient to claim that  $\sigma(500)$  is present but some contribution can also not be excluded. Its integrated fractional contribution to the Dalitz plot is estimated to  $\sim 3\%$ . In solution 18, the  $S_3 = f_0(1370)$  is removed additionally, with leads to a  $\chi^2$  increase of 0.44 units while two parameters are spared; the  $f_0(1370)$  does not help to improve the fit. If  $f_0(1500)$  is removed (Sol. 19),  $\chi^2$  increases by 7.67. In solution 20,

$f_0(1710)$  is removed, and  $\chi^2$  changes by 3.77 units. Again,  $f_0(1500)$  has the largest impact on the fit quality. The best  $\chi^2$  per degree of freedom is achieved when the scalar wave is described by  $f_0(980)$ ,  $f_0(1500)$ , and  $f_0(1710)$ .

Instead of using masses and widths from [18], we may chose values given in the PDG listings. The overall  $\chi^2$  deteriorates by 2 units; the  $\chi^2$  changes remain close to the ones shown in Tables 9 and 10. When the  $f_0(1370)$  parameters are changed, mass and width can adopt nearly arbitrary values. Its parameters cannot be deduced from this data. A free fit to  $f_0(1710)$  properties puts its mass to the limit of the phase space, with a marginal  $\chi^2$  improvement.

The fractional contributions of the various isobars to the Dalitz plot are not well defined quantities. First, interference effects make it impossible to assign a fraction of a data to an *amplitude*. The second argument is more technical: the fit fraction depends on the model used. Tables 7, 8 and 9, 10 show the spread of results when the fit hypothesis is varied. From solution 14 we estimate that nearly 70% of the intensity comes from  $f_0(980)$ , 8% from  $f_0(1500)$ , 8% from  $\rho(1450)$ , and 15% from  $f_2(1270)$ .

#### 4.5 Mass scans

In mass scans, the mass of one resonance is changed in steps, and the change of  $\chi^2$  as a function of the imposed

mass is inspected. In a well behaved situation, the  $\chi^2$  distribution exhibits a local minimum at the optimal mass.

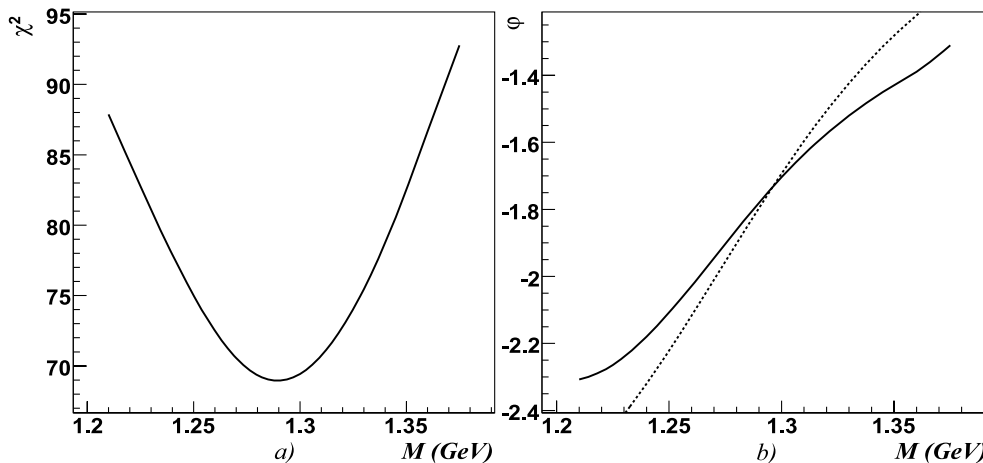
The resonance is produced with an arbitrary phase relative to the production of another meson. When the mass of the physical meson under study and the Breit–Wigner test mass coincide (and their respective widths), the Breit–Wigner amplitude and phase, and amplitude and phase of the physical resonance agree over the full mass range of the resonance. The overall phase difference of the resonances under study relative to the other mesons is determined in the fit; this phase is denoted here as  $\varphi_0$ . When the test mass is changed, the Breit–Wigner amplitude and phase do no longer match the complex amplitude in the data. In this situation, the fitted amplitude adjusts its phase in a way that the true phase and the fitted phase match in the mass range in which the true resonance and the test Breit–Wigner amplitude have a large overlap. In a mass scan, the phase motion is thus approximately reproduced by the fitted phase. This method was developed in [19]; a first application showed that the  $\eta(1440)$  region hosts one un-split resonance [20]. The analytical form of a Breit–Wigner amplitude leads to an overall sign change of the amplitude when going far below the nominal mass to far above the resonance, independent of its coupling to other channels, independent of inelasticities.

The method explores directly the phase of a Breit–Wigner amplitude.

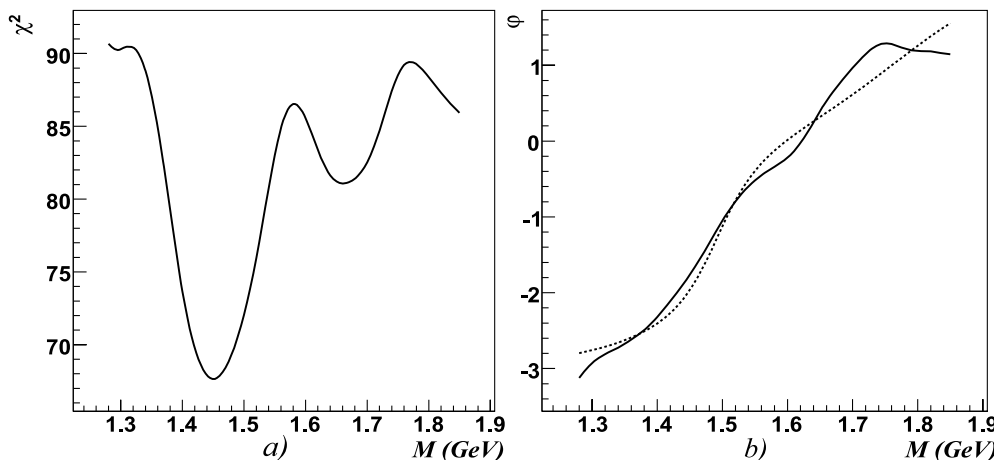
We test this idea by monitoring the phase of the  $f_2(1270)$ . Figure 6 shows a scan of the  $f_2$  mass region. The minimum in  $\chi^2$  reached at 1280 MeV (see Fig. 6b). The ‘observed’ phase resulting from the fit shows a strong variation as a function of the imposed  $f_2$  mass, stronger than expected for a single Breit–Wigner. A phase variation is observed as expected but quantitatively, the expected phase variation is not reproduced. This may serve as a warning that the method is not without risk.

Figure 7a shows the scan of a scalar amplitude. We start from solution 13 of Table 9, fix the mass of the scalar meson at pre-set values, and determine the  $\chi^2$  as a function of the pre-set mass. The scalar mass is varied from 1.2 to 1.7 GeV/ $c^2$ . A deep minimum in  $\chi^2$  is observed at  $M = 1452 \pm 22$  MeV/ $c^2$  reproducing findings of previous analyses. At a mass of 1680 MeV, a weaker but still pronounced local minimum is seen which we tentatively identify with  $f_0(1710)$ . The mass shift with respect to the expected value is possibly due to the phase space limitation.

The phase motion observed in the scan and shown in Fig. 7b exhibits a surprise: in the range from 1.2 to 1.7 GeV/ $c^2$  it covers more than  $2\pi$ . The region must house more than a single resonance. This result encouraged us to



**Fig. 6.** **a**  $\chi^2$  of a fit in which the mass of the  $f_2(1270)$  is scanned. **b** The associated phase as a function of the mass



**Fig. 7.** **a**  $\chi^2$  of a fit which includes  $f_0(980)$ ,  $\rho(1450)$ , and  $f_2(1270)$  with fixed masses and widths and one scalar resonance the mass of which is scanned. The width of this resonance is fixed to 110 MeV. **b** The scalar phase motion as derived from the fit (solid line). The fitted scalar phase motion (dashed line) assumes two additional scalar resonances,  $f_0(1500)$  and  $f_0(1710)$

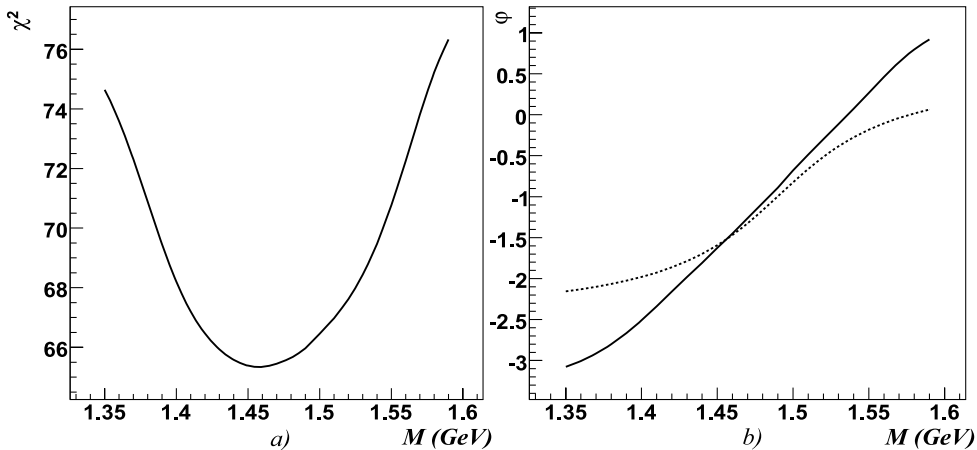


**Fig. 8.** **a**  $\chi^2$  of a fit which includes  $f_0(980)$ ,  $\rho(1450)$ ,  $f_2(1270)$ , and  $f_0(1710)$  with fixed masses and widths and one scalar resonance the mass of which is scanned. The width of this resonance is fixed to 110 MeV. **b** The scalar phase motion as derived from the fit (solid line). The fitted scalar phase motion (dashed line) assumes one additional scalar resonance,  $f_0(1500)$ . The ‘observed’ phase motion covers a wider range than a single resonance does

introduce a  $f_0(1710)$  with fixed parameters. The phase motion expected for two resonances (plus a small contribution from  $f_0(980)$ ) agrees reasonably well with the ‘measured’ phase, see Fig. 7b.

As a next step, we include  $f_0(1710)$  in the fit with fixed parameters and study the remaining scalar wave in a scan with a second scalar resonance. The result is shown in Fig. 8a, the associated phase motion in Fig. 8b. There is now one  $\chi^2$  minimum which is wider than the central minimum seen in Fig. 7a. When  $f_0(1710)$  is added, the mass uncertainty increases, and the fit yields  $M = 1470 \pm 60 \text{ MeV}/c^2$ , a value which is not incompatible with 1500 MeV. If instead of  $f_0(1710)$  the  $f_0(1370)$  resonance is included, the production strength of the second scalar resonance gets small, and the  $\chi^2$  minimum is found at 1400 MeV. Obviously, the interference of two close-by resonances can mimic the observed structure but we discard this solution.

The phase motions shown in Figs. 7b and 8b are suggestive but should be discussed with some reservations. The observed phase is certainly influenced by the data but the fit does not determine the local phase. The phase is derived from a comparison of data and a Breit–Wigner amplitude of finite (110 MeV) width; thus, the phase motion is smeared out. Second, the phase is determined from fits in which the mass of the resonance under studied is in-

tentionally detuned. It is hence not guaranteed that the fit does not explore different local minima. In order to test the method, we have made the scans with different widths of the test Breit–Wigner amplitude (with  $\Gamma = 60$  or  $160 \text{ MeV}/c^2$ ). No significant changes were found supporting the hypothesis that the observed phase motions reflect some physics content.

Thus we go one step beyond, and try to determine the number of resonances by comparing the observed phase motions with Breit–Wigner phase motions of resonances with fixed masses and widths. In Fig. 9, the ‘observed’ phase motion of Fig. 7 is shown together with two fits. Both fits use  $f_0(1500)$  and  $f_0(1710)$ , fit (a) adds  $f_0(1370)$ , fit (b) adds the wide background amplitude  $f_0(1000)$  suggested by Au, Morgan, and Pennington [14], and by Minkowski and Ochs [15]. Both possibilities reproduce the ‘observed’ phase shift reasonably well even though  $f_0(1370)$  leads to an expected phase motion exceeding slightly the observed one while introducing  $f_0(1000)$  leads to a perfect match.

We have tried to perform a mass-independent analysis by choosing complex amplitudes for the scalar partial wave in each mass bin, and offering these to the minimization process. This mass independent partial wave amplitude was partly restricted to 2, 3, or 4 mass bins. The results were unstable; we failed to derive a mass independent partial wave amplitude from these studies.

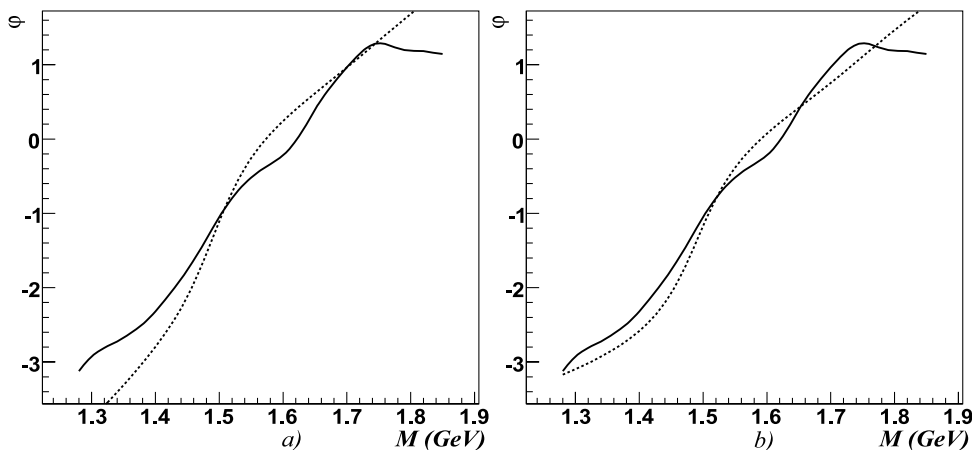


**Fig. 9.** The scalar phase motion as derived from the fit (solid line). The fitted scalar phase motion (dashed line) assumes three additional scalar resonances. In **a**, these are  $f_0(1370)$ ,  $f_0(1500)$ , and  $f_0(1710)$ ; in **b**  $f_0(1000)$ ,  $f_0(1500)$ , and  $f_0(1710)$ , where  $f_0(1000)$  represents the wide scalar background discussed in the text

## 5 Discussion and conclusions

We have studied the Dalitz plot for  $D_s^+$  decays into  $\pi^-\pi^+\pi^+$ . In agreement with earlier findings, we found that the largest fraction of the data stems from scalar isoscalar mesons decaying into  $\pi^-\pi^+$ , in particular the  $f_0(980)$  meson. The  $\rho(1460)$  and  $f_2(1270)$  contribute significantly as well. We have made the attempt to understand the conflicting results on scalar mesons which were obtained from fits to the  $D_s^+ \rightarrow \pi^-\pi^+\pi^+$  Dalitz plot. Previous fits agree that the data require scalar intensity in the mass region above the  $f_0(980)$ . When fitted with a Breit–Wigner amplitude, an optimal mass between 1440 and 1475 MeV/ $c^2$  was found. The masses quoted were not compatible with the mass of neither the  $f_0(1370)$  – which we rather assume to have 1320 MeV/ $c^2$  – nor with the  $f_0(1500)$  resonance. Thus it is often argued that both,  $f_0(1370)$  and  $f_0(1500)$ , might be required to get a good fit when nominal (PDG) masses and widths are imposed.

We reproduce these results. However, when a high mass resonance,  $f_0(1710)$ , is introduced, the  $f_0(1500)$  resonance alone is sufficient to yield an acceptable fit. The  $\chi^2$  as a function of the assumed scalar mass of the  $f_0(1370)/f_0(1500)$  develops a flat floor, and the  $1\sigma$  mass interval extends from 1.41 to 1.53 MeV/ $c^2$ . Thus the observed mass is fully compatible with the hypothesis that the standard  $f_0(1500)$  is produced in the reaction. An additional contribution from a  $f_0(1370)$  resonance is not required. If the existence of  $f_0(1370)$  is assumed, its parameters can be chosen to agree with the ‘narrow’  $f_0(1370)$  of the PDG or with the ‘wide’ red dragon of Minkowsky and Ochs. The statistics we used is not sufficient to discriminate between the three alternatives ‘no  $f_0(1370)$ ’, ‘wide  $f_0(1370)$ ’, or ‘narrow  $f_0(1370)$ ’. The  $\sigma(500)$  leads to a marginal improvement of the fit, with a statistical evidence just above one standard deviation. In the  $K$ -matrix fits, the inclusion of the  $f_0(1370)$  resonance was necessary in fits to a large body of different reactions. In the fits to the  $D_s \rightarrow 3\pi$  data,  $f_0(1370)$  does provide a notable improvement even though this data alone is not sufficient to claim its existence.

One could dream of future high-statistics high-quality data. There is however the possibility to combine existing data from different experiments. The reaction  $D_s^+ \rightarrow \pi^-\pi^+\pi^+$  was studied at Fermilab by the E687 (434 events) [7], E791 (848 events) [8] and the FOCUS (1475 events) [9, 10] collaborations. The BaBar collaboration has extracted 2900 events; preliminary results were reported in a PhD thesis at Bochum [21]. Including Belle results, a factor 10 can be reached in statistics. The dif-

ferent background contributions would help to understand the systematic errors. We urge that enterprize should be undertaken.

*Acknowledgements.* We thank the E791 collaboration for providing us with their data described in [1], for simulations of their detector (for acceptance corrections) and for other related discussions. Helpful comments by B. Meadows and A. Correa dos Reis are particularly acknowledged. M.M. was supported by a grant from the Deutsche Forschungsgemeinschaft.

## References

1. E791 Collaboration, E.M. Aitala et al., Phys. Rev. Lett. **86**, 770 (2001)
2. CLEO Collaboration, H. Muramatsu et al., Phys. Rev. Lett. **89**, 251802 (2002)
3. CLEO Collaboration, H. Muramatsu et al., Phys. Rev. Lett. **90**, 059901 (2003) [Erratum]
4. E791 Collaboration, E.M. Aitala et al., Phys. Rev. Lett. **89**, 121801 (2002)
5. E791 Collaboration, E.M. Aitala et al., Phys. Rev. D **73**, 032004 (2006)
6. E791 Collaboration, E.M. Aitala et al., Phys. Rev. D **74**, 059901 (2006) [Erratum]
7. E687 Collaboration, P.L. Frabetti et al., Phys. Lett. B **407**, 79 (1997)
8. E791 Collaboration, E.M. Aitala et al., Phys. Rev. Lett. **86**, 765 (2001)
9. FOCUS Collaboration, J.M. Link et al., Phys. Lett. B **585**, 200 (2004)
10. FOCUS Collaboration, S. Malvezzi, AIP Conf. Proc. **717**, 77 (2004)
11. D. Asner, Review of Charm Dalitz plot analyses, see [12]
12. Particle Data Group, W.M. Yao et al., J. Phys. G **33**, 1 (2006)
13. P. Estabrooks, Phys. Rev. D **19**, 2678 (1979)
14. K.L. Au, D. Morgan, M.R. Pennington, Phys. Rev. D **35**, 1633 (1987)
15. P. Minkowski, W. Ochs, Eur. Phys. J. C **9**, 283 (1999)
16. E. Klempt, A. Zaitsev, Phys. Rep. **454**, 1 (2007)
17. E791 Collaboration, E.M. Aitala et al., Eur. Phys. J. direct C **1**, 4 (1999)
18. V.V. Anisovich, A.V. Sarantsev, Eur. Phys. J. A **16**, 229 (2003)
19. E. Klempt, A.V. Anisovich, V.A. Nikonov, A.V. Sarantsev, U. Thoma, Eur. Phys. J. A **29**, 307 (2006)
20. E. Klempt, The glueball candidate  $\eta(1440)$  as  $\eta$  radial excitation, arXiv:hep-ph/0409148
21. T. Deppermann, Resonanzstruktur des Zerfalls  $D_s^\pm$  decays into  $\pi^-\pi^+\pi^\pm$ , PhD thesis, University of Bochum, 2002